GEOPHYSICS, VOL. 88, NO. 3 (MAY-JUNE 2023); P. 1–10, 13 FIGS., 1 TABLE.
10.1190/GEO2022-0321.1

Anelastic dispersion and attenuation of P- and SV-wave scattering by aligned nonisothermal inclusions of finite thickness

Jia Wei[1], Li-Yun Fu[2], José M. Carcione[3], and Wubing Deng[2]

ABSTRACT

1 We have investigated the anelastic dispersion and attenu-
2 ation of P- and SV-wave scattering by nonisothermal inclusions of finite thickness. The inclusions, which are aligned and sparsely embedded in an isotropic medium, induce an initial static stress field (acoustoelasticity) and a nonlinear dependence of the velocities on this stress. Moreover, we describe the anelastic properties as a function of frequency by incorporating the displacement discontinuities across the inclusion into the representation theorem by using the Foldy approximation. The response as a function of temperature is calculated for different incidence angles (anisotropy), and the results find that anelasticity increases with an increasing temperature difference between the inclusions and the background medium. The SV wave in the solid inclusions indicates a stronger sensitivity along the inclusion normal, and it is more affected than the P wave. The P- and SV-wave scattering by fluid-saturated inclusions behave in an opposite manner. This theory can be useful to evaluate the distribution of temperature from seismic attributes.

INTRODUCTION

Thermoelastic stress produced by a nonuniform temperature distribution within the earth is recognized as an important source of stress that affects its tectonic history. The effects of thermoelastic stress have been identified in media with inclusions. It is found that the geoid profiles of fracture zones show significant bending due to thermoelastic stress (Parmentier and Haxby, 1986; Haxby and Parmentier, 1988). The thermoelastic stresses resulting from thermal anomalies can alter the permeability of the rock (e.g., Patterson et al., 2018). Seismic prospecting is extensively used to image these inclusions and also provide information about their pressure-temperature
conditions. Therefore, it is important to study the effects of those 3
stresses, associated with temperature distributions, on seismic attributes, especially the dispersion and attenuation of seismic waves.

Many models have been proposed for seismic dispersion and attenuation in heterogeneous media. Early works focus on elastic scattering by a single dry inclusion in an isotropic homogeneous medium (e.g., Mal, 1970a, 1970b; Martin, 1981; Krenk and Schmidt, 1982). Many papers accurately describe the scattering processes in isotropic or anisotropic media (e.g., Crampin, 1978; Sánchez Sesma and Iturrarán Viveros, 2001). Based on the Foldy approximation (Foldy, 1945), the elastic scattering by a set of randomly and homogeneously distributed dry inclusions has been investigated (e.g., Kikuchi, 1981; Yamashita, 1990; Kawahara, 1992). This approach has been used to develop several models for wave scattering by aligned fluid-saturated inclusions in nonporous (e.g., Kawahara and Yamashita, 1992; Guo et al., 2018b) and porous media (e.g., Galvin and Gurevich, 2006; Song et al., 2017; Fu et al., 2018, 2020; Guo et al., 2018a).

Elastic scattering and thermoelasticity are two distinct wave dissipation mechanisms (Aki, 1980; Sato et al., 2012). Thermoelasticity describes the coupling between elastic deformation and temperature, by which temperature fluctuations lead to wave dissipation (Biot, 1956). This theory is relevant in geothermal exploration (e.g., Armstrong, 1984; Cermak et al., 1990; Fu, 2012, 2017) and earth-
quake seismology (e.g., Simmons and Brace, 1965; Boschi, 1973). 4
The classic theory, based on a parabolic-type equation of heat conduction, predicts unphysical solutions, that is, infinite velocities. The Lord-Shulman model avoids this problem (Lord and Shulman, 1967) by introducing a relaxation time into the heat-conduction equation. Rudgers (1990) analyzes the theory of wave propagation, and Carcione et al. (2018, 2019) compute synthetic seismograms based

Manuscript received by the Editor 11 May 2022; revised manuscript received 18 November 2022; published ahead of production 13 February 2023.
[1]Chinese Academy of Sciences, Key Laboratory of Petroleum Resource Research, Institute of Geology and Geophysics, Beijing, China; University of Chinese Academy of Sciences, Beijing, China; and Chinese Academy of Sciences, Innovation Academy for Earth Science, Beijing, China. E-mail: jiawei@mail.iggcas.ac.cn.
[2]China University of Petroleum (East China), Key Laboratory of Deep Oil and Gas, Qingdao, China and Qingdao National Laboratory for Marine Science and Technology, Laboratory for Marine Mineral Resources, Qingdao, China. E-mail: lfu@upc.edu.cn (corresponding author); wubing.deng@foxmail.com.
[3]National Institute of Oceanography and Applied Geophysics (OGS), Trieste, Italy. E-mail: jcarcione@inogs.it.

on this model, the latter being a generalization to the poroelastic case. The corresponding frequency-domain Green function has been derived by Wang et al. (2019) and Wei et al. (2020a). Moreover, Wei et al. (2020b) study the thermoelastic dispersion and attenuation of P- and SV-wave scattering by aligned inclusions in an isothermal elastic medium. Wei et al. (2022) recently investigated the coupling between a wave-induced thermal flux and elastic scattering based on the Lord and Shulman equations of dynamic thermoelasticity.

A medium with a nonuniform temperature distribution can be subjected to a prestressed environment induced by thermoelastic stress (e.g., Parmentier and Haxby, 1986; Zhu and Wiens, 1991; Patterson et al., 2018). The seismic wave velocity of most cracked rocks is very sensitive to initial static stress (Cheng and Toksöz, 1979; Zimmerman et al., 1986). A theory called acoustoelasticity describes the stress-induced variations in elastic-wave velocity through the third-order elastic constants, which can be estimated from the slope obtained by a linear relationship law between the elastic moduli and applied stress (Winkler and Liu, 1996; Winkler and McGowan, 2004). Prioul et al. (2004) calculate the third-order elastic constants in the low- and high-prestressed environment, respectively, demonstrating higher third-order elastic constants at low stress. The nonlinear relation between the rock elastic modulus and the loaded pressure due to mechanical defects (such as microstructure) has been well demonstrated by experimental measurements (e.g., Johnson and McCall, 1994; Sinha and Plona, 2001; David and Zimmerman, 2012).

We describe the elastic deformation of nonisothermal inclusions by combining the thermoelasticity and acoustoelasticity theories to model wave scattering. First, we obtain the stresses from a 2D rectangular inclusion. Then, we follow Wei et al. (2020b) and estimate the dispersion and attenuation of the P and SV waves induced by the displacement discontinuities in inclusions constrained by the acoustoelasticity boundary condition as a result of thermoelastic stresses. Finally, the variation of these properties with regard to temperature and incidence angle is analyzed.

MODEL FORMULATION

Wei et al. (2020b) investigate the P- and SV-wave scattering by the aligned isothermal fluid-saturated inclusions of finite thickness. The model of inclusions extends the model of Kawahara (1992) to the case of wet cracks and that of Guo et al. (2018b) to include shear waves. In this study, we extend the model to the nonisothermal inclusions containing solid or fluid with a negligible background porosity. The model is shown in Figure 1, where the number of aligned inclusions per unit area, called inclusion number density ν, is small. The 3D problem can be reduced to a 2D problem if we assume that all of the inclusions are parallel to the x_1-axis but infinitely long along the x_3-axis. An incident plane wave of angular frequency ω at an angle φ (or ϕ) with respect to the x_2-axis is considered. The theory includes not only the conventional scattering mechanism but also the acoustoelasticity effect caused by thermoelastic stresses across the inclusion boundaries.

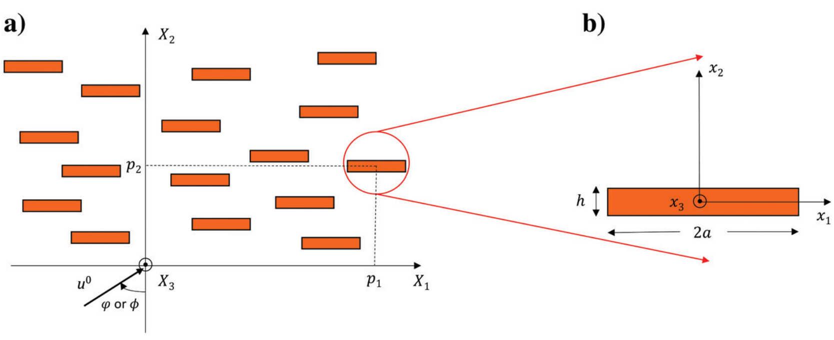

Figure 1. Sparsely and homogeneously nonisothermal aligned inclusions of the same shape embedded in an isotropic elastic medium. These solid/fluid-saturated inclusions are parallel to the x_1-axis but infinitely long along the x_3-axis, have thickness h and half-length a, and are centered at (p_1, p_2), the origin of the local coordinate system (x_1, x_2). Symbol u^0 denotes an incident harmonic plane wave P (or SV) at an angle φ (or ϕ) measured from the x_2-axis. A similar model has been used by Kawahara (1992) with aligned dry open cracks, Guo et al. (2018b) with aligned fluid-saturated cracks of finite thickness, and Wei et al. (2020b) with aligned isothermal fluid-saturated inclusions of finite thickness.

Thermoelastic stresses from a 2D rectangular inclusion

The stress components σ_{ij} of a thermoelastic medium are (Biot, 1956; Carcione et al., 2020; Wei et al., 2020b)

$$\sigma_{ij} = \lambda\delta_{ij}\theta + \mu u_{i,j} + \mu u_{j,i} - (3\lambda + 2\mu)\alpha\delta_{ij}T, \qquad (1)$$

where λ and μ are the Lamé constants, δ_{ij} is the Kronecker-delta components, θ is the volumetric strain, u_i is the displacement component, T is the increment of temperature above a reference absolute temperature T_0, and α is the coefficient of thermal expansion. Substituting equation 1 into the equations of equilibrium yields

$$(\lambda + \mu)\theta_{,i} + \mu u_{i,jj} - (3\lambda + 2\mu)\alpha T_{,i} = 0. \qquad (2)$$

Introducing the thermoelastic displacement potential $\Psi_{,i} = u_i$, equation 2 becomes

$$(\lambda + 2\mu)\Psi_{,ijj} = (3\lambda + 2\mu)\alpha T_{,i}. \qquad (3)$$

Integrating equation 3 with respect to x_i, we obtain

$$\left(\frac{\partial^2}{\partial x_1^2} + \frac{\partial^2}{\partial x_2^2} + \frac{\partial^2}{\partial x_3^2}\right)\Psi = \frac{3\lambda + 2\mu}{\lambda + 2\mu}\alpha T. \qquad (4)$$

Similarly, the 2D thermoelastic displacement potential is

$$\left(\frac{\partial^2}{\partial x_1^2} + \frac{\partial^2}{\partial x_2^2}\right)\Psi = \frac{3\lambda + 2\mu}{2(\lambda + \mu)}\alpha T. \qquad (5)$$

Based on the displacement potential $\Psi_{,i} = u_i$ and equation 4, the stress components σ_{ij} can be transformed to

$$\sigma_{ij} = 2\mu(\Psi_{,ij} - \Psi_{,kk}\delta_{ij}). \qquad (6)$$

Assuming that the temperature difference $T = T^{(i)} - T_0$ between the inclusion and surrounding medium is constant, and the internal and external elastic properties and thermal expansion coefficients are the same within a certain temperature range, equation 5 becomes

$$\left(\frac{\partial^2}{\partial x_1^2}+\frac{\partial^2}{\partial x_2^2}\right)$$

$$\Psi=\begin{cases}\frac{3\lambda+2\mu}{2(\lambda+\mu)}\alpha T, & -a<x_1<a \text{ and } -\frac{h}{2}<x_2<\frac{h}{2}\\ 0, & x_1\langle -a \text{ or } x_1\rangle a \text{ or } x_2\left\langle -\frac{h}{2} or x_2\right\rangle \frac{h}{2}\end{cases}. \quad (7)$$

According to the potential theory, the particular solution to equation 7 is

$$\Psi(x_1,x_2)=\frac{3\lambda+2\mu}{4\pi(\lambda+\mu)}\alpha T\int_{\xi_1=-a}^{a}\int_{\xi_2=-\frac{h}{2}}^{\frac{h}{2}}\ln r d\xi_1 d\xi_2, \quad (8)$$

where $r^2=(x_1-\xi_1)^2+(x_2-\xi_2)^2$.

By substituting this solution into equation 6, we obtain the following thermoelasticity stress components:

$$\begin{cases}\sigma_{11}^{\mathrm{T}}=-\frac{3\lambda+2\mu}{2(\lambda+\mu)}\frac{\alpha T\mu}{\pi}\left\{\left(\tan^{-1}\frac{x_1-a}{x_2-\frac{h}{2}}-\tan^{-1}\frac{x_1+a}{x_2-\frac{h}{2}}\right)-\left(\tan^{-1}\frac{x_1-a}{x_2+\frac{h}{2}}-\tan^{-1}\frac{x_1+a}{x_2+\frac{h}{2}}\right)\right\}\\ \sigma_{22}^{\mathrm{T}}=-\frac{3\lambda+2\mu}{2(\lambda+\mu)}\frac{\alpha T\mu}{\pi}\left\{\left(\tan^{-1}\frac{x_2-\frac{h}{2}}{x_1-a}-\tan^{-1}\frac{x_2+\frac{h}{2}}{x_1-a}\right)-\left(\tan^{-1}\frac{x_2-\frac{h}{2}}{x_1+a}-\tan^{-1}\frac{x_2+\frac{h}{2}}{x_1+a}\right)\right\}\\ \sigma_{33}^{T}=-\frac{2(3\lambda+2\mu)}{\lambda+2\mu}\alpha T\mu\\ \sigma_{12}^{\mathrm{T}}=\frac{3\lambda+2\mu}{2(\lambda+\mu)}\frac{\alpha T\mu}{\pi}\mathrm{In}\frac{\sqrt{(x_1-a)^2+\left(x_2-\frac{h}{2}\right)^2}\cdot\sqrt{(x_1+a)^2+\left(x_2+\frac{h}{2}\right)^2}}{\sqrt{(x_1-a)^2+\left(x_2+\frac{h}{2}\right)^2}\cdot\sqrt{(x_1+a)^2+\left(x_2-\frac{h}{2}\right)^2}}\\ \sigma_{13}^{T}=\sigma_{23}^{T}=0\end{cases} \quad (9)$$

If the length of the inclusion is much larger than its thickness, the terms σ_{11}^{T}, σ_{22}^{T}, and σ_{12}^{T} are very small compared with σ_{33}^{T} and can be neglected within the inclusion. It can be considered that the inclusion is only affected by the stress in the x_3-direction.

The aligned nonisothermal inclusion model

Wei et al. (2020b) model the anelasticity of P and SV waves by aligned isothermal inclusions. Appendix A derives the dispersion/attenuation coefficient. Unlike aligned isothermal inclusions, nonisothermal inclusions generate axial thermoelastic stress in the x_3-direction, mentioned in the "Thermoelastic stresses from a 2D rectangular inclusion" section, which results in a high-order constitutive relation between the applied stress and resulting strain. This effect, called acoustoelasticity, yields velocities dependent on the stress state of the medium.

For nonisothermal solid inclusion with a small aspect ratio, the normal and shear stresses become (Pao, 1984)

$$\begin{cases}\sigma_{12}^{E}+\sigma_{12}^{S}=\left(\mu-P\frac{m-\frac{\lambda+\mu}{2\mu}n-2\lambda}{3\lambda+2\mu}\right)\frac{[\Delta\vec{u}_{ni}(x_1,p_1,p_2)]_1}{h}\\ \sigma_{22}^{E}+\sigma_{22}^{S}=\left(\lambda+2\mu-P\frac{2l-\frac{2\lambda}{\mu}(\lambda+2\mu+m)}{3\lambda+2\mu}\right)\frac{[\Delta\vec{u}_{ni}(x_1,p_1,p_2)]_2}{h}\end{cases}, \ |x_1|<a, x_2=0, \quad (10)$$

where σ_{jk}^{E} and σ_{jk}^{S} are the stress components caused by $\langle\vec{u}_{ni}\rangle$ and $S_{nj}\langle\vec{u}_{ni}\rangle$, respectively; $S_{nj}\langle\vec{u}_{ni}\rangle$ is the scattered wavefield at the njth inclusion by averaging the incident wavefield $\vec{u}_{ni}$ of the nith inclusion; and l, m, and n are third-order elastic moduli. By combining the axial stress $P=-\sigma_{33}^{\mathrm{T}}$ and equation 10, we obtain the following boundary conditions:

$$\begin{cases}\sigma_{12}^{E}+\sigma_{12}^{S}=\left(\mu-2\alpha T\mu\frac{m-\frac{\lambda+\mu}{2\mu}n-2\lambda}{\lambda+2\mu}\right)\frac{[\Delta\vec{u}_{ni}(x_1,p_1,p_2)]_1}{h}\\ \sigma_{22}^{E}+\sigma_{22}^{S}=\left(\lambda+2\mu-2\alpha T\mu\frac{2l-\frac{2\lambda}{\mu}(\lambda+2\mu+m)}{\lambda+2\mu}\right)\frac{[\Delta\vec{u}_{ni}(x_1,p_1,p_2)]_2}{h}\end{cases}, \ |x_1|<a, x_2=0. \quad (11)$$

Substituting equations A-3 and A-6 into equation 11 yields

$$\begin{cases}\int_{-a}^{a}T_{121}(x_1,0|\xi_1,0)D_1(\xi_1)d\xi_1+\frac{\mu-2\alpha T\mu\frac{m-\frac{\lambda+\mu}{2\mu}n-2\lambda}{\lambda+2\mu}}{\mu h}D_1(x_1)=e^{ik_{\mathrm{P}}x_1\sin\varphi}\\ \int_{-a}^{a}T_{222}(x_1,0|\xi_1,0)D_2(\xi_1)d\xi_1+\frac{\lambda+2\mu-2\alpha T\mu\frac{2l-\frac{2\lambda}{\mu}(\lambda+2\mu+m)}{\lambda+2\mu}}{\mu h}D_2(x_1)=e^{ik_{\mathrm{P}}x_1\sin\varphi}\end{cases}, \quad (12)$$

where T_{jkl} is given in Kawahara and Yamashita (1992) and D_j is given in equation A-9. The method of Yamashita (1990) is adopted to solve for D_j numerically. Therefore, equation 12 becomes

$$\begin{cases}\int_{-1}^{1}\hat{\mathrm{T}}_{121}(s,0|\hat{\xi}_1,0)\hat{\mathrm{D}}_1(\hat{\xi}_1)d\hat{\xi}_1+\frac{\mu-2\alpha T\mu\frac{m-\frac{\lambda+\mu}{2\mu}n-2\lambda}{\lambda+2\mu}}{\mu h}\hat{\mathrm{D}}_1(s)=e^{i\hat{\mathrm{k}}_{\mathrm{P}}s\sin\varphi}\\ \int_{-1}^{1}\hat{\mathrm{T}}_{222}(s,0|\hat{\xi}_1,0)\hat{\mathrm{D}}_2(\hat{\xi}_1)d\hat{\xi}_1+\frac{\lambda+2\mu-2\alpha T\mu\frac{2l-\frac{2\lambda}{\mu}(\lambda+2\mu+m)}{\lambda+2\mu}}{\mu h}\hat{\mathrm{D}}_2(s)=e^{i\hat{\mathrm{k}}_{\mathrm{P}}s\sin\varphi}\end{cases}, \quad (13)$$

which is discretized as

$$\begin{cases}\sum_{n=1}^{M-1}\left(T_{mn}^{121}+\frac{\mu-2\alpha T\mu\frac{m-\frac{\lambda+\mu}{2\mu}n-2\lambda}{\lambda+2\mu}}{\mu h}\delta_{mn}\right)\hat{\mathrm{D}}_{1n}=e^{i\hat{\mathrm{k}}_{\mathrm{P}}s_m\sin\varphi}\\ \sum_{n=1}^{M-1}\left(T_{mn}^{222}+\frac{\lambda+2\mu-2\alpha T\mu\frac{2l-\frac{2\lambda}{\mu}(\lambda+2\mu+m)}{\lambda+2\mu}}{\mu h}\delta_{mn}\right)\hat{\mathrm{D}}_{2n}=e^{i\hat{\mathrm{k}}_{\mathrm{P}}s_m\sin\varphi}\end{cases}, \ m=1,\ldots,M-1. \quad (14)$$

Here, $\hat{\mathrm{D}}_j(j=1,2)$ can be calculated from equation 14. Then, we obtain the dispersion/attenuation coefficient κ_{P} for P-wave scattering from $\hat{\mathrm{D}}_j(j=1,2)$ and equation A-13. The phase velocity V_{P} and dissipation factor Q_{P}^{-1} are (Kawahara and Yamashita, 1992)

$$\begin{cases}V_{\mathrm{P}}=\left(1-\mathrm{Re}\,\kappa_{\mathrm{P}}\frac{\cos\varphi}{k_{\mathrm{P}}}\right)v_{\mathrm{P}}\\ Q_{\mathrm{P}}^{-1}=2\,\mathrm{Im}\,\kappa_{\mathrm{P}}\frac{\cos\varphi}{k_{\mathrm{P}}}\end{cases}, \quad (15)$$

where Re and Im denote the real and imaginary parts, respectively. Similarly, we obtain κ_{SV} from equation A-16, and

$$\begin{cases}V_{\mathrm{SV}}=\left(1-\mathrm{Re}\,\kappa_{\mathrm{SV}}\frac{\cos\phi}{k_{\mathrm{SV}}}\right)v_{\mathrm{SV}}\\ Q_{\mathrm{SV}}^{-1}=2\,\mathrm{Im}\,\kappa_{\mathrm{SV}}\frac{\cos\phi}{k_{\mathrm{SV}}}\end{cases}. \quad (16)$$

For nonisothermal fluid-saturated inclusion, the normal and shear stresses become (Kostek et al., 1993)

$$\begin{cases}\sigma_{12}^{E}+\sigma_{12}^{S}=0\\ \sigma_{22}^{E}+\sigma_{22}^{S}=\left(\lambda_f-P\frac{4l_f-2m_f+n_f}{2\lambda_f}\right)\frac{[\Delta\vec{u}_{ni}(x_1,p_1,p_2)]_2}{h}\end{cases}. \quad (17)$$

Because the third-order elastic moduli l_f, m_f, and n_f of the fluid are very small compared with the Lamé constant λ_f, the acoustoelasticity effect in the fluid-saturated inclusion can be neglected. Moreover, the thermoelastic effect behaves significantly for fluid inclusion, which differs from solid inclusion (Wei et al., 2020b). Considering the thermoelastic effect on the nonisothermal fluid-saturated inclusion yields the following normal and shear stresses (Wei et al., 2020b):

$$\begin{cases} \sigma_{12}^E + \sigma_{12}^S = 0 \\ \sigma_{22}^E + \sigma_{22}^S = \left(\lambda_f + \frac{9\lambda_f^2 \alpha_f^2 T^{(i)}}{\rho_f C_f}\right) \frac{[\Delta \vec{u}_{ni}(x_1, p_1, p_2)]_2}{h}, \end{cases} \quad |x_1| < a, x_2 = 0, \tag{18}$$

where α_f, ρ_f, and C_f are the thermal expansion coefficient, mass density, and specific heat capacity of the fluid, respectively. Similarly, we can obtain the dispersion/attenuation coefficient for P- and SV-wave scattering by the aligned nonisothermal fluid-saturated inclusions.

Table 1. Fluid properties at different temperatures.

T_0 (°K)	α_f (10^{-6}/°K)	ρ_f (kg/m^3)	C_f (m^2/[s^2 · °K])	λ_f (MPa)
348	195.4	1007.3	4050.0	2701.0
398	264.8	975.2	4090.0	2401.1
498	431.1	889.7	4246.0	1520.8

NUMERICAL EXAMPLES

Some numerical examples illustrate P- and SV-wave dissipation in a nonisothermal media containing inclusions with negligible background porosity. We consider the following inclusion number density, half-length, and thickness: 4×10^{-5} m^{-2}, 50 m, and 2 m, respectively. The wave dissipation is analyzed for two sets of inclusion parameters: (1) solid properties with $\lambda = 4$ GPa, $\mu = 6$ GPa, $\alpha = 0.33 \times 10^{-5}$°K^{-1}, $\rho = 2650$ kg/m^3, $l = -295$ GPa, $m = -997$ GPa, and $n = -1672$ GPa at 298°K (Winkler and McGowan, 2004; Carcione et al., 2018), which are assumed to be constant within a certain temperature range and (2) fluid properties at different temperatures shown in Table 1 (Kretzschmar and Wagner, 2019). After obtaining the value of the dispersion/attenuation coefficient κ from these parameters, the phase velocity and dissipation factor can be calculated from equations 15 and 16.

We show the phase velocity of the SV-wave scattering by the solid-inclusion model as a function of frequency at various incidence angles in ($\phi = 0°$) Figure 2a, ($\phi = 60°$) Figure 2b, and ($\phi = 90°$) Figure 2c for three different temperature differences. The velocity is almost constant at low frequencies, because of Rayleigh scattering, and then increases rapidly at the middle-frequency Mie scattering range, and slightly as a result of high-frequency scattering. Increasing the temperature difference, the velocity dispersion becomes stronger in the low- and middle-frequency regimes, especially in the first, whereas the effect in the high-frequency regime is negligible. Moreover, at high incidence angles, the dispersion is weak. To further

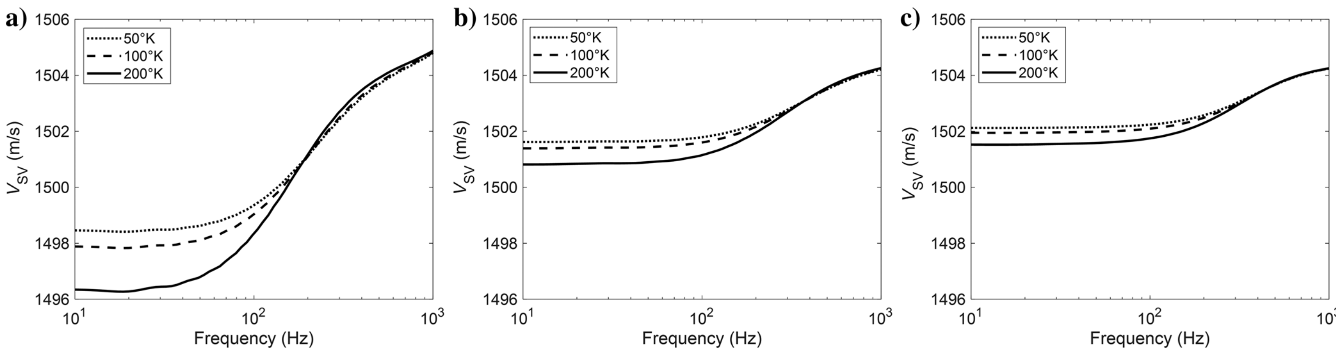

Figure 2. Phase velocity of the SV-wave scattering by the solid-inclusion model as a function of frequency at ϕ = (a) 0°, (b) 60°, and (c) 90° for three temperature differences.

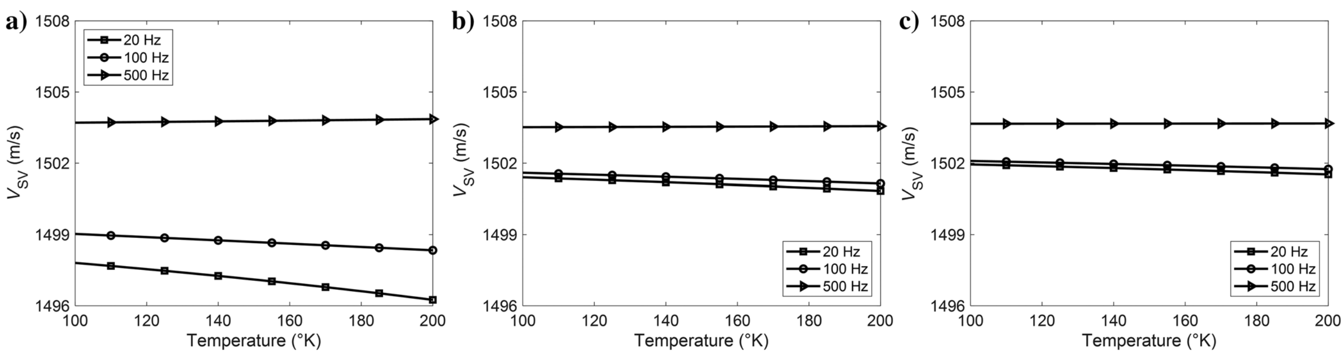

Figure 3. Phase velocity of the SV-wave scattering by the solid-inclusion model as a function of the temperature difference at ϕ = (a) 0°, (b) 60°, and (c) 90° for three frequencies.

illustrate the effect of the temperature difference, Figure 3 shows the SV-wave dispersion at $\varphi = 0°$ (Figure 3a), 60° (Figure 3b), and 90° (Figure 3c) for the three frequencies (20, 100, and 500 Hz) corresponding to Rayleigh, Mie, and high-frequency scattering, respectively. The effects are more pronounced at low frequencies.

Figure 4 shows the dissipation factor of the SV-wave scattering by the solid-inclusion model as a function of frequency. It has the shape of a relaxation peak, and the effect of the temperature difference is
5 pronounced at frequencies around the peak. The attenuation decreases with increasing the incidence angle and exhibits greater sensitivity than dispersion, that is, stronger anisotropy. The dissipation factor of the SV wave as a function of the temperature difference at $\phi = 0°$ (Figure 4a), 60° (Figure 4b), and 90° (Figure 4c) for the three frequencies is shown in Figure 5. Attenuation increases with increasing the temperature difference. This is because the thermoelastic stress is positively correlated with the temperature difference and the acoustoelastic effect increases with the stress. When the inclusion temperature is higher than the background temperature, the acoustoelastic effect reduces the wave velocity and enhances the scattering attenuation because of the reduction in inclusion stiffness.

Figures 6, 7, 8, and 9 display the same quantities as Figures 2–5, 6
respectively, but for the P wave at $\varphi = 0°$ (Figures 6a, 7a, 8a, and

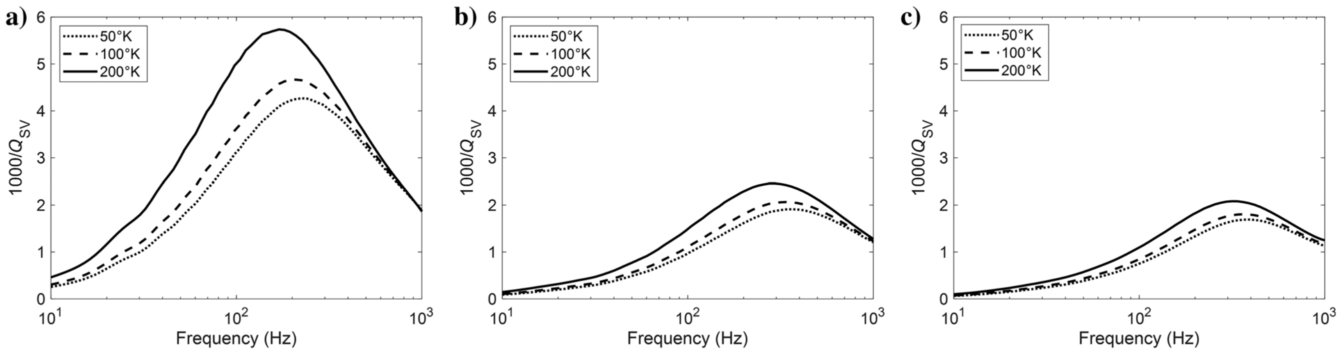

Figure 4. Dissipation factor of the SV-wave scattering by the solid-inclusion model as a function of frequency at ϕ = (a) 0°, (b) 60°, and (c) 90° for three temperature differences.

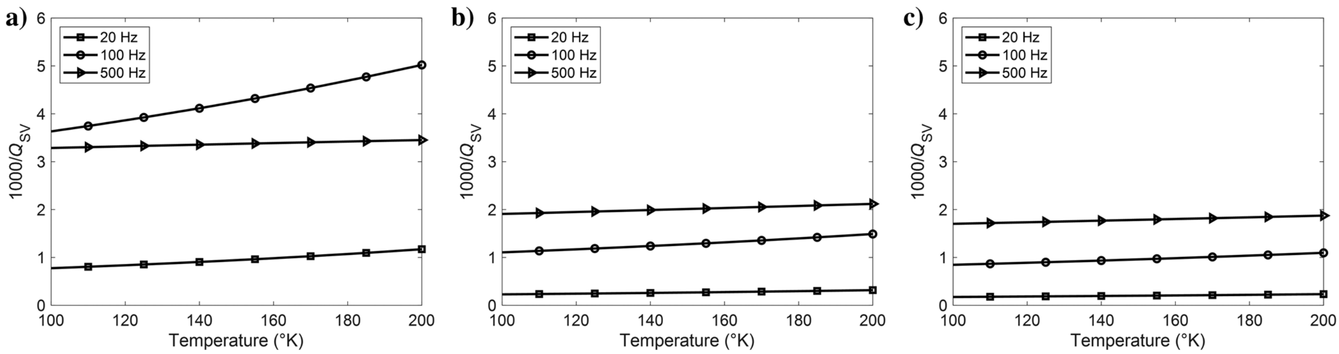

Figure 5. Dissipation factor of the SV-wave scattering by the solid-inclusion model as a function of the temperature difference at ϕ = (a) 0°, (b) 60°, and (c) 90° for three frequencies.

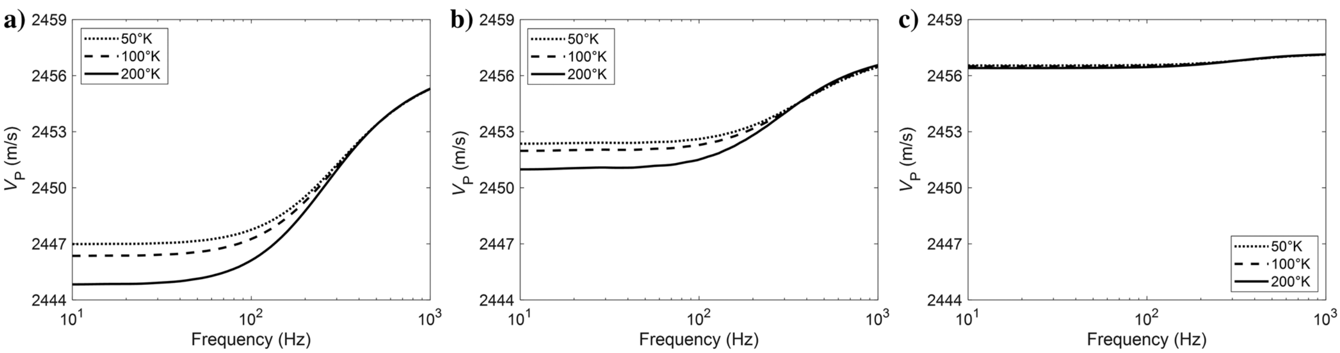

Figure 6. Same as Figure 2, but for the P wave at ϕ = (a) 0°, (b) 60°, and (c) 90°.

9a), 60° (Figures 6b, 7b, 8b, and 9b), and 90° (Figures 6c, 7c, 8c, and 9c). The trend is similar, but there are differences in magnitude with a temperature difference due to the acoustoelastic effect, which reduces the shear modulus across the inclusions as a result of the thermal stress. For example, the P-wave dispersion and attenuation curves are almost independent of the temperature differences at $\varphi = 90°$ compared with those of the SV wave.

7 Figures 10 and 11 show the same quantities as Figures 2 and 4, respectively, but for the SV-wave scattering by the fluid-saturated inclusion model at $\phi = 0°$ (Figures 10a and 11a), 60° (Figures 10b and 11b), and 90° (Figures 10c and 11c). Because the temperature fluctuations in the fluid model do not cause shear stress, and the polarization direction of the SV wave is orthogonal to the propagation direction, the SV wave for the three temperature differences along the direction normal to the inclusions results in the same dispersion and attenuation. Unlike the case of normal incidence, shown in Fig- 8
ures 10b, 10c, 11b, and 11c, the SV-wave dispersion and attenuation vary with temperature, which decreases with increasing the incidence angle. Figures 12 and 13 display the same quantities as Figures 10 and 11, respectively, but for the P wave at $\varphi = 0°$ (Figures 12a and 13a), 60° (Figures 12b and 13b), and 90° (Figures 12c and 13c). Similar to the SV wave, the P-wave dispersion and attenuation decrease with increasing the incidence angle. Compared with the SV wave, the variations of the P-wave dispersion and attenuation are more pronounced as a function of the temperature difference but show less sensitivity to the incidence angle.

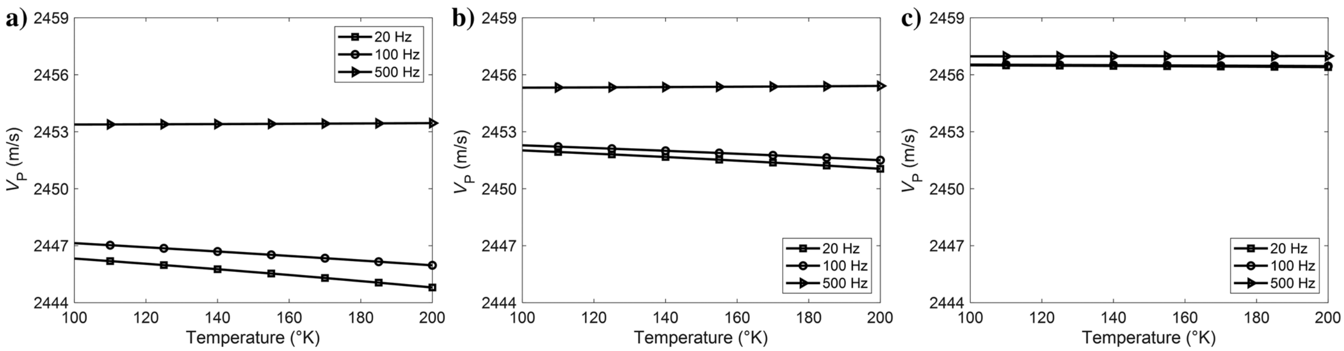

Figure 7. Same as Figure 3, but for the P wave at ϕ = (a) 0°, (b) 60°, and (c) 90°.

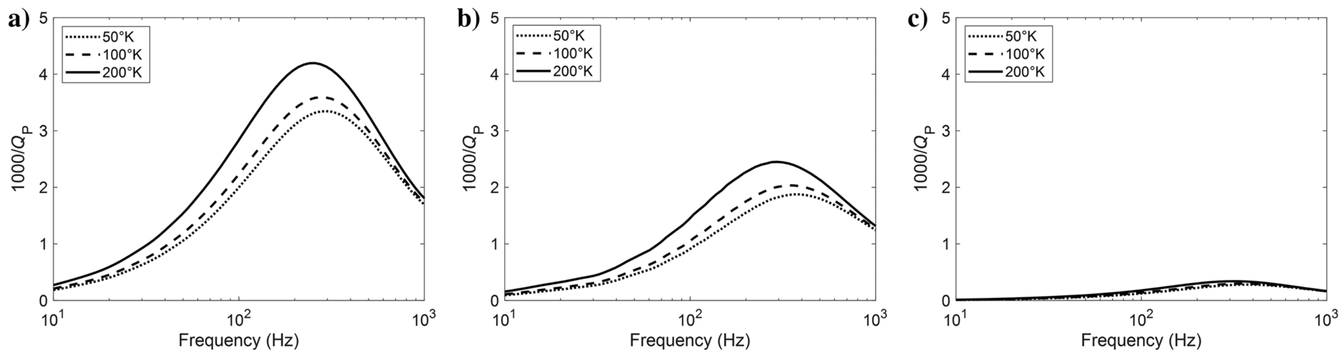

Figure 8. Same as Figure 4, but for the P wave at ϕ = (a) 0°, (b) 60°, and (c) 90°.

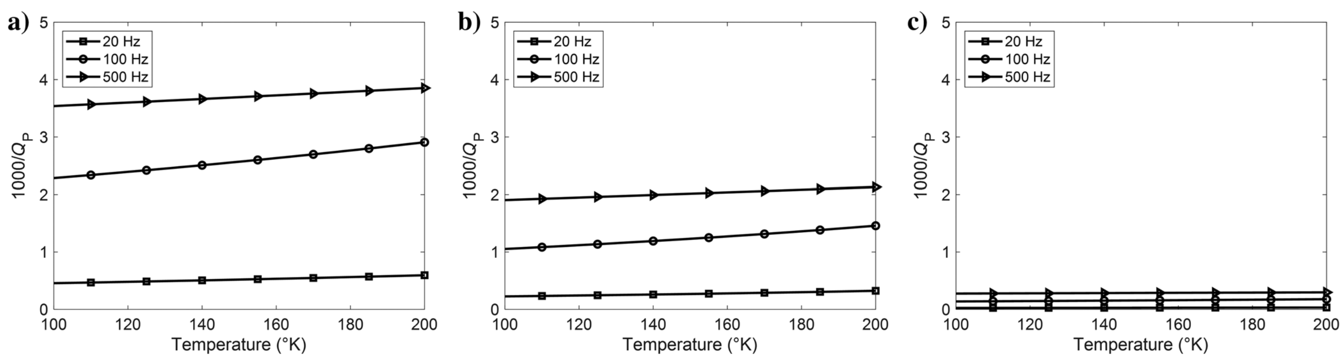

Figure 9. Same as Figure 5, but for the P wave at ϕ = (a) 0°, (b) 60°, and (c) 90°.

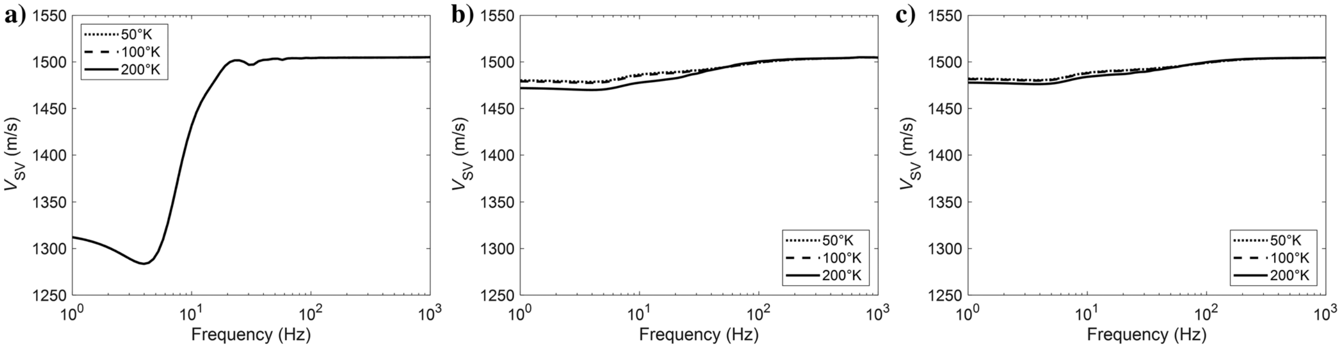

Figure 10. Same as Figure 2, but for the SV-wave scattering by the fluid-saturated inclusion model at ϕ = (a) 0°, (b) 60°, and (c) 90°.

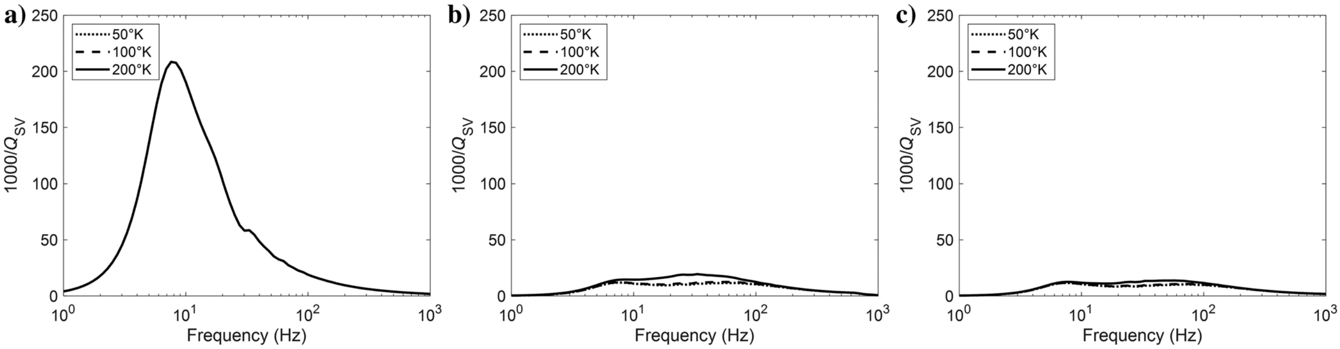

Figure 11. Same as Figure 4, but for the SV-wave scattering by the fluid-saturated inclusion model at ϕ = (a) 0°, (b) 60°, and (c) 90°.

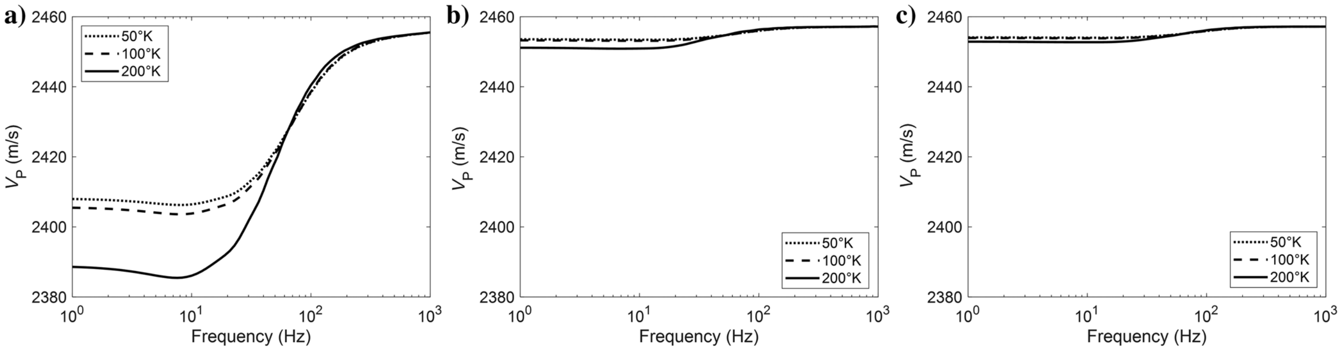

Figure 12. Same as Figure 10, but for the P wave at ϕ = (a) 0°, (b) 60°, and (c) 90°.

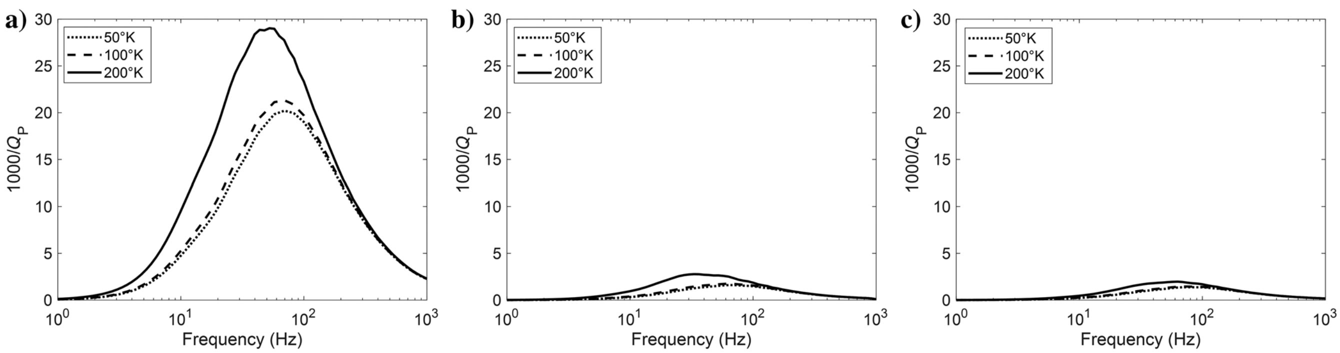

Figure 13. Same as Figure 11, but for the P wave at ϕ = (a) 0°, (b) 60°, and (c) 90°.

DISCUSSION

In this paper, we describe the relation between seismic dissipation and nonisothermal inclusions with an impermeable background where the thermal anomaly propagates solely via diffusion instead of convection. Thermal effects can exchange between the background and 9 inclusion by the convection in a permeable host rock (Patterson and Driesner, 2021), which are not considered in our model. To study this effect, we can extend this model to the fluid-saturated porous background medium based on the thermo-poroelasticity theory (Carcione et al., 2019; Wei et al., 2020a).

In addition to wave scattering and thermal effects, wave-induced fluid flow (WIFF) also will occur for a fluid-saturated porous background with cracks, leading to the additional dispersion and attenuation of the seismic waves. In general, wave dissipation in the low-frequency range is dominated by thermal effects and WIFF, whereas the scattering determines the high-frequency range, but we also need to consider the nonlinear coupling between these mechanisms (Guo and Gurevich, 2020; Wei et al., 2022).

The present theory can be supplemented with other models to estimate temperature distribution, water content, and rock composition (Romanowicz and Mitchell, 2007; Carcione et al., 2020). A limitation of our model is only valid for the sparsely distributed inclusions, and it is necessary to extend it to the dense case in the future (e.g., Benites et al., 1992).

CONCLUSION

We have developed a model to estimate the effects of nonisothermal aligned inclusions on wave anelasticity. The effects on the P and SV waves not only include the elastic scattering but also the acoustoelastic effect by thermoelastic stresses across inclusion boundaries, based on the Foldy approximation. Then, we evaluate the seismic dispersion and attenuation as a function of temperature and incidence angle. The results indicate that the dissipation increases with the increasing temperature difference between the inclusions and background medium. The SV-wave scattering by the solid-inclusion model shows a strong sensitivity to this difference along the direction perpendicular to the inclusions, whereas the P wave is less affected. However, the P and SV waves in the fluid-saturated inclusion model behave in the opposite manner.

ACKNOWLEDGMENTS

The research is supported by the National Natural Science Foundation of China (grant nos. 42230803 and 41821002) and the 111 project "Deep-Superdeep Oil & Gas Geophysical Exploration" (B18055). No experimental data are used in this paper.

DATA AND MATERIALS AVAILABILITY

Data associated with this research are available and can be obtained by contacting the corresponding author.

APPENDIX A

DISPERSION/ATTENUATION COEFFICIENTS FOR MODELS OF SCATTERING BY ALIGNED ISOTHERMAL SOLID INCLUSIONS

The mean wavefield $\vec{u}_A$ at the observation point **A** is the sum of the incident wavefield $\vec{u}^{\,0}_A$ and the scattered wavefield $\vec{S}_A\langle\vec{u}_{ni}\rangle$ as

$$\langle\vec{u}_A\rangle = \vec{u}^{\,0}_A + \nu\int\vec{S}_A\langle\vec{u}_{ni}\rangle d\vec{r}_{ni} \quad \text{(A-1)}$$

for aligned inclusions distributed sparsely and randomly through a 2D homogeneous medium, where $\langle\vec{u}_{ni}\rangle$ is the mean incident wavefield at the $n$ith inclusion and $\vec{r}_{ni} = (p_1, p_2)$ denotes the central location of this inclusion. For the incident P wave, we consider

$$\vec{u}^{\,0}_A = A_0 e^{ik_P X_1 \sin\varphi + ik_P X_2 \cos\varphi}(\sin\varphi, \cos\varphi) \quad \text{(A-2)}$$

with amplitude A_0, wavenumber $k_P = \omega/v_P$, and velocity v_P of the background medium. The mean incident wavefield $\langle\vec{u}_A\rangle$ at the observation point **A** is

$$\langle\vec{u}_A\rangle = Ae^{ik_P X_1 \sin\varphi + ik_P X_2(\cos\varphi + \kappa_P/k_P)}\left(\sin\varphi, \cos\varphi + \frac{\kappa_P}{k_P}\right) \quad \text{(A-3)}$$

with the unknown mean wavefield amplitude A and an unknown coefficient κ_P describing the dispersion and attenuation. The jth component of the scattered wavefield $\vec{S}_{nj}\langle\vec{u}_{ni}\rangle$ at the njth inclusion by the mean incident wavefield $\langle\vec{u}_{ni}\rangle$ of the nith inclusion is

$$[\vec{S}_{nj}\langle\vec{u}_{ni}\rangle]_j = -\int_{-a}^{a}[\Delta\vec{u}_{ni}(\xi_1, p_1, p_2)]_l \Gamma_{jl}(x_1, x_2|\xi_1, 0)d\xi_1, \quad j, l = 1, 2, \quad \text{(A-4)}$$

where $[\Delta\vec{u}_{ni}(\xi_1, p_1, p_2)]_l$ is the lth component of the displacement discontinuity through the nith inclusion, and the Green function stress tensor Γ_{jl} is

$$\begin{aligned}\Gamma_{jl}(x_1,x_2|\xi_1,\xi_2) &= \frac{i}{4}\left[\delta_{l2}\left(1-2\frac{k_P^2}{k_{SV}^2}\right)\frac{\partial}{\partial x_j}H_0^{(1)}(k_P R)\right.\\ &+\left(\delta_{jl}\frac{\partial}{\partial x_2}+\delta_{j2}\frac{\partial}{\partial x_l}\right)H_0^{(1)}(k_{SV}R)-\frac{2}{k_{SV}^2}\frac{\partial^3}{\partial x_j\partial x_l\partial x_2}\\ &\left.(H_0^{(1)}(k_P R)-H_0^{(1)}(k_{SV}R))\right],\quad j,l=1,2,\end{aligned} \quad \text{(A-5)}$$

where $k_{SV} = \omega/v_{SV}$ and v_{SV} are the wavenumber and wave velocity of the background medium, respectively; $R = \sqrt{(x_1-\xi_1)^2 + (x_2-\xi_2)^2}$; and $H_0^{(1)}(kR)$ is the zero-order Hankel function of the first kind. From equation A-4 and Hooke's law, the stress caused by $\langle\vec{u}_{ni}\rangle$ and $\vec{S}_{nj}\langle\vec{u}_{ni}\rangle$ is (Kawahara and Yamashita, 1992; Guo et al., 2018b)

$$\begin{cases}\sigma^E_{jk} = \lambda\delta_{jk}\frac{\partial}{\partial x_l}[\langle\vec{u}_{ni}\rangle]_l + \mu\left(\frac{\partial}{\partial x_k}[\langle\vec{u}_{ni}\rangle]_j + \frac{\partial}{\partial x_j}[\langle\vec{u}_{ni}\rangle]_k\right)\\ \sigma^S_{jk} = -\mu\int_{-a}^{a}[\Delta\vec{u}_{ni}(\xi_1,p_1,p_2)]_l T_{jkl}(x_1,x_2|\xi_1,0)d\xi_1\end{cases},\quad j,k,l=1,2, \quad \text{(A-6)}$$

where λ and μ are the Lamé constants of the background medium.

For solid inclusions with a small aspect ratio, the normal and shear stresses are

$$\begin{cases}\sigma^E_{12} + \sigma^S_{12} = \mu_c\frac{[\Delta\vec{u}_{ni}(x_1,p_1,p_2)]_1}{h}\\ \sigma^E_{22} + \sigma^S_{22} = (\lambda_c + 2\mu_c)\frac{[\Delta\vec{u}_{ni}(x_1,p_1,p_2)]_2}{h}\end{cases},\quad |x_1| < a, x_2 = 0. \quad \text{(A-7)}$$

Substituting equations A-3 and A-6 into equation A-7 yields

$$\begin{cases} \int_{-a}^{a} T_{121}(x_1,0|\xi_1,0)D_1(\xi_1)d\xi_1 + \frac{\mu_c}{\mu h}D_1(x_1) = e^{ik_{\mathrm{P}}x_1 \sin\varphi} \\ \int_{-a}^{a} T_{222}(x_1,0|\xi_1,0)D_2(\xi_1)d\xi_1 + \frac{\lambda_c+2\mu_c}{\mu h}D_2(x_1) = e^{ik_{\mathrm{P}}x_1 \sin\varphi} \end{cases}, \ |x_1|<a, \tag{A-8}$$

where the T_{jkl} is given in the paper by Kawahara and Yamashita (1992) and

$$\begin{cases} D_1(\xi_1) = \frac{[\Delta\vec{u}_{ni}(\xi_1,p_1,p_2)]_1}{2i(k_{\mathrm{P}}\cos\varphi+\kappa_{\mathrm{P}})\sin\varphi A e^{ik_{\mathrm{P}}p_1\sin\varphi+ik_{\mathrm{P}}p_2(\cos\varphi+\kappa_{\mathrm{P}}/k_{\mathrm{P}})}} \\ D_2(\xi_1) = \frac{[\Delta\vec{u}_{ni}(\xi_1,p_1,p_2)]_2}{ik_{\mathrm{P}}Ae^{ik_{\mathrm{P}}p_1\sin\varphi+ik_{\mathrm{P}}p_2(\cos\varphi+\kappa_{\mathrm{P}}/k_{\mathrm{P}})}\left[\left(\frac{k_{\mathrm{SV}}^2}{k_{\mathrm{P}}^2}-2\right)\sin^2\varphi+\frac{k_{\mathrm{SV}}^2}{k_{\mathrm{P}}^2}\left(\cos\varphi+\frac{\kappa_{\mathrm{P}}}{k_{\mathrm{P}}}\right)^2\right]} \end{cases}. \tag{A-9}$$

The method of Yamashita (1990) is adopted to solve for D_j numerically; thus, equation A-8 is transformed into

$$\begin{cases} \int_{-1}^{1} \hat{\mathrm{T}}_{121}(s,0|\hat{\xi}_1,0)\hat{\mathrm{D}}_1(\hat{\xi}_1)d\hat{\xi}_1 + \frac{\mu_c}{\mu h}\hat{\mathrm{D}}_1(s) = e^{i\hat{\mathrm{k}}_{\mathrm{P}}s\sin\varphi} \\ \int_{-1}^{1} \hat{\mathrm{T}}_{222}(s,0|\hat{\xi}_1,0)\hat{\mathrm{D}}_2(\hat{\xi}_1)d\hat{\xi}_1 + \frac{\lambda_c+2\mu_c}{\mu h}\hat{\mathrm{D}}_2(s) = e^{i\hat{\mathrm{k}}_{\mathrm{P}}s\sin\varphi} \end{cases}, \ |s|<1, \tag{A-10}$$

which is discretized as

$$\begin{cases} \sum_{n=1}^{M-1}\left(T_{mn}^{121}+\frac{\mu_c}{\mu h}\delta_{mn}\right)\hat{\mathrm{D}}_{1n} = e^{i\hat{\mathrm{k}}_{\mathrm{P}}s_m\sin\varphi} \\ \sum_{n=1}^{M-1}\left(T_{mn}^{222}+\frac{\lambda_c+2\mu_c}{\mu h}\delta_{mn}\right)\hat{\mathrm{D}}_{2n} = e^{i\hat{\mathrm{k}}_{\mathrm{P}}s_m\sin\varphi} \end{cases}, \ m=1,\ldots,M-1, \tag{A-11}$$

where $s_m = -1 + m\Delta s$, $\Delta s = 2/M$, M is the discretization number, and $\hat{\mathrm{D}}$ is approximately constant in the nth interval:

$$\begin{cases} \hat{\xi}_1 = \frac{\xi_1}{a}, s = \frac{x_1}{a}, \hat{\mathrm{k}}_{\mathrm{P}} = ak_{\mathrm{P}} \\ \hat{\mathrm{T}}_{j2j} = a^2T_{j2j}, \hat{\mathrm{D}}_j = \frac{D_j}{a}, j=1,2 \end{cases}, \tag{A-12}$$

and $T_{mn}^{j2j} = \int_{s_n-\Delta s/2}^{s_n+\Delta s/2}\hat{\mathrm{T}}_{j2j}(s_m,0|\hat{\xi}_1,0)d\hat{\xi}_1 \quad (j=1,2)$. Here, $\hat{\mathrm{D}}_j(j=1,2)$ and $[\Delta u_{ni}]_j(j=1,2)$ can be obtained from equations A-11 and A-9, respectively, and then we can obtain $[S_{nj}\langle\vec{u}_{ni}\rangle]_j$. Substituting $[S_{nj}\langle\vec{u}_{ni}\rangle]_j$ and equation A-2 into equation A-1, compared with equation A-3, yields

$$\kappa_{\mathrm{P}} = \nu k_{\mathrm{P}}a^2[\hat{\phi}_1 f\sin 2\varphi\sin\varphi + \frac{\hat{\phi}_2}{2f\cos\varphi}(1-2f\sin^2\varphi)^2] \tag{A-13}$$

with $f = v_{\mathrm{SV}}^2/v_{\mathrm{P}}^2$ and $\hat{\phi}_j = \sum_{m=1}^{M-1}\hat{\mathrm{D}}_{jm}e^{-i\hat{\mathrm{k}}_{\mathrm{P}}s_m\sin\varphi}\Delta s(j=1,2)$.

10 For the incident SV wavefield $\vec{u}_{\mathrm{A}}^0$, we consider

$$\vec{u}_{\mathrm{A}}^0 = B_0e^{ik_{\mathrm{SV}}X_1\sin\phi+ik_{\mathrm{SV}}X_2\cos\phi}(\cos\phi,-\sin\phi), \tag{A-14}$$

where B_0 is the amplitude and the wavenumber k_{SV} is defined as ω/v_{SV}. The mean wavefield $\vec{u}_{\mathrm{A}}$ at the observation point **A** is

$$\langle\vec{u}_{\mathrm{A}}\rangle = Be^{ik_{\mathrm{SV}}X_1\sin\phi+ik_{\mathrm{SV}}X_2(\cos\phi+\kappa_{\mathrm{SV}}/k_{\mathrm{SV}})} \times\left(\cos\phi+\frac{\kappa_{\mathrm{SV}}}{k_{\mathrm{SV}}},-\sin\phi\right), \tag{A-15}$$

where B is the amplitude of the unknown average wavefield and κ_{SV} is the unknown coefficient describing the dispersion and attenuation. Then, we obtain

$$\kappa_{\mathrm{SV}} = \nu k_{\mathrm{SV}}a^2\left[\hat{\phi}_1\frac{\cos^2 2\phi}{2\cos\phi}+\hat{\phi}_2\sin 2\phi\sin\phi\right]. \tag{A-16}$$

REFERENCES

Aki, K., 1980, Attenuation of shear-waves in the lithosphere for frequencies from 0.05 to 25 Hz: Physics of the Earth and Planetary Interiors, **21**, 50–60, doi: 10.1016/0031-9201(80)90019-9.

Armstrong, B. H., 1984, Models for thermoelastic attenuation of waves in heterogeneous solids: Geophysics, **49**, 1032–1040, doi: 10.1190/1.1441718.

Benites, R., K. Aki, and K. Yomogida, 1992, Multiple scattering of SH waves in 2-D media with many cavities: Pure and Applied Geophysics, **138**, 353–390, doi: 10.1007/BF00876878.

Biot, M. A., 1956, Thermoelasticity and irreversible thermodynamics: Journal of Applied Physics, **27**, 240–253, doi: 10.1063/1.1722351.

Boschi, E., 1973, A thermoviscoelastic model of the earthquake source mechanism: Journal of Geophysical Research, **78**, 7733–7737, doi: 10.1029/JB078i032p07733.

Carcione, J. M., F. Cavallini, E. Wang, J. Ba, and L. Y. Fu, 2019, Physics and simulation of wave propagation in linear thermo-poroelastic media: Journal of Geophysical Research, **124**, 8147–8166, doi: 10.1029/2019JB017851.

Carcione, J. M., B. Farina, F. Poletto, A. N. Qadrouh, and W. Cheng, 2020, Seismic attenuation in partially molten rocks: Physics of the Earth and Planetary Interiors, **309**, 106568, doi: 10.1016/j.pepi.2020.106568.

Carcione, J. M., Z. W. Wang, W. Ling, E. Salusti, J. Ba, and L. Y. Fu, 2018, Simulation of wave propagation in linear thermoelastic media: Geophysics, **84**, no. 1, T1–T11, doi: 10.1190/geo2018-0448.1.

Cermak, V., L. Bodri, L. Rybach, and G. Buntebarth, 1990, Relationship between seismic velocity and heat production: Comparison of two sets of data and test of validity: Earth and Planetary Science Letters, **99**, 48–57, doi: 10.1016/0012-821X(90)90069-A.

Cheng, C. H., and M. N. Toksöz, 1979, Inversion of seismic velocities for the pore aspect ratio spectrum of a rock: Journal of Geophysical Research: Solid Earth, **84**, 7533–7543, doi: 10.1029/JB084iB13p07533.

Crampin, S., 1978, Seismic-wave propagation through a cracked solid: Polarization as a possible dilatancy diagnostic: Geophysical Journal International, **53**, 467–496, doi: 10.1111/j.1365-246X.1978.tb03754.x.

David, E. C., and R. W. Zimmerman, 2012, Pore structure model for elastic wave velocities in fluid-saturated sandstones: Journal of Geophysical Research: Solid Earth, **117**, B07210, doi: 10.1029/2012JB009195.

Foldy, L. L., 1945, The multiple scattering of waves. I. General theory of isotropic scattering by randomly distributed scatters: Physical Review, **67**, 107, doi: 10.1103/PhysRev.67.107.

Fu, B. Y., L. Y. Fu, J. Guo, R. J. Galvin, and B. Gurevich, 2020, Semi-analytical solution to the problem of frequency dependent anisotropy of porous media with an aligned set of slit cracks: International Journal of Engineering Science, **147**, 103209, doi: 10.1016/j.ijengsci.2019.103209.

Fu, B. Y., J. Guo, L. Y. Fu, S. Glubokovskikh, R. J. Galvin, and B. Gurevich, 2018, Seismic dispersion and attenuation in saturated porous rock with aligned slit cracks: Journal of Geophysical Research: Solid Earth, **123**, 6890–6910, doi: 10.1029/2018JB015918.

Fu, L. Y., 2012, Evaluation of sweet spot and geopressure in Xihu sag: Tech report, CCL2012-SHPS-0018ADM, Key Laboratory of Petroleum Resource Research, Institute of Geology and Geophysics, Chinese Academy of Sciences.

Fu, L. Y., 2017, Deep-superdeep oil gas geophysical exploration 111: Program report jointly initiated by MOE and SAFEA, B18055, School of Geosciences China University of Petroleum (East China).

Galvin, R. J., and B. Gurevich, 2006, Interaction of an elastic wave with a circular crack in a fluid-saturated porous medium: Applied Physics Letters, **88**, 061918, doi: 10.1063/1.2165178.

Guo, J., J. Germán Rubino, N. D. Barbosa, S. Glubokovskikh, and B. Gurevich, 2018a, Seismic dispersion and attenuation in saturated porous rocks with aligned fractures of finite thickness: Theory and numerical simulations — Part 1: P-wave perpendicular to the crack plane: Geophysics, **83**, no. 1, WA49–WA62, doi: 10.1190/geo2017-0065.1.

Guo, J., and B. Gurevich, 2020, Effects of coupling between wave-induced fluid flow and elastic scattering on P-wave dispersion and attenuation in rocks with aligned fractures: Journal of Geophysical Research: Solid Earth, **125**, e2019JB018685, doi: 10.1029/2019JB018685.
Guo, J., D. Shuai, J. Wei, P. Ding, and B. Gurevich, 2018b, P-wave dispersion and attenuation due to scattering by aligned fluid saturated fractures with finite thickness: Theory and experiment: Geophysical Journal International, **215**, 2114–2133, doi: 10.1093/gji/ggy406.
Haxby, W. F., and E. M. Parmentier, 1988, Thermal contraction and the state of stress in the oceanic lithosphere: Journal of Geophysical Research: Solid Earth, **93**, 6419–6429, doi: 10.1029/JB093iB06p06419.
Johnson, P. A., and K. R. McCall, 1994, Observation and implications of nonlinear elastic wave response in rock: Geophysical Research Letters, **21**, 165–168, doi: 10.1029/93GL03162.
Kawahara, J., 1992, Scattering of P, SV waves by random distribution of aligned open cracks: Journal of Physics of the Earth, **40**, 517–524, doi: 10.4294/jpe1952.40.517.
Kawahara, J., and T. Yamashita, 1992, Scattering of elastic waves by a fracture zone containing randomly distributed cracks: Pure and Applied Geophysics, **139**, 121–144, doi: 10.1007/BF00876828.
Kikuchi, M., 1981, Dispersion and attenuation of elastic waves due to multiple scattering from cracks: Physics of the Earth and Planetary Interiors, **27**, 100–105, doi: 10.1016/0031-9201(81)90037-6.
Kostek, S., B. K. Sinha, and A. N. Norris, 1993, Third-order elastic constants for an inviscid fluid: The Journal of the Acoustical Society of America, **94**, 3014–3017, doi: 10.1121/1.407336.
Krenk, S., and H. Schmidt, 1982, Elastic wave scattering by a circular crack: Philosophical Transactions of the Royal Society of London. Series A, Mathematical and Physical Sciences, **308**, 167–198, doi: 10.1098/rsta.1982.0158.
Kretzschmar, H. J., and W. Wagner, 2019, International steam tables: Properties of water and steam based on the industrial formulation IAPWS-IF97: Springer.
Lord, H. W., and Y. Shulman, 1967, A generalized dynamical theory of thermoelasticity: Journal of the Mechanics and Physics of Solids, **15**, 299–309, doi: 10.1016/0022-5096(67)90024-5.
Mal, A. K., 1970a, Interaction of elastic waves with a penny-shaped crack: International Journal of Engineering Science, **8**, 381–388, doi: 10.1016/0020-7225(70)90075-3.
Mal, A. K., 1970b, Interaction of elastic waves with a Griffith crack: International Journal of Engineering Science, **8**, 763–776, doi: 10.1016/0020-7225(70)90003-0.
Martin, P. A., 1981, Diffraction of elastic waves by a penny-shaped crack: Proceedings of the Royal Society of London. A. Mathematical and Physical Sciences, **378**, 263–285, doi: 10.1098/rspa.1981.0151.
Pao, Y. H., 1984, Acoustoelasticity and ultrasonic measurement of residual stress: Physical Acoustics, **15**, 61–143.
Parmentier, E. M., and W. F. Haxby, 1986, Thermal stresses in the oceanic lithosphere: Evidence from geoid anomalies at fracture zones: Journal of Geophysical Research: Solid Earth, **91**, 7193–7204, doi: 10.1029/JB091iB07p07193.
Patterson, J. W., and T. Driesner, 2021, Elastic and thermoelastic effects on thermal water convection in fracture zones: Journal of Geophysical Research: Solid Earth, **126**, e2020JB020940, doi: 10.1029/2020JB020940.
Patterson, J. W., T. Driesner, S. Matthai, and R. Tomlinson, 2018, Heat and fluid transport induced by convective fluid circulation within a fracture or fault: Journal of Geophysical Research: Solid Earth, **123**, 2658–2673, doi: 10.1002/2017JB015363.
Prioul, R., A. Bakulin, and V. Bakulin, 2004, Nonlinear rock physics model for estimation of 3D subsurface stress in anisotropic formations: Theory and laboratory verification: Geophysics, **69**, 415–425, doi: 10.1190/1.1707061.
Romanowicz, B., and B. Mitchell, 2007, Deep earth structure: *Q* of the Earth from crust to core: Treatise on Geophysics, **1**, 731–774, doi: 10.1016/B978-044452748-6.00024-9.
Rudgers, A. J., 1990, Analysis of thermoacoustic wave propagation in elastic media: Journal of the Acoustical Society of America, **88**, 1078–1094, doi: 10.1121/1.399856.
Sánchez Sesma, F. J., and U. Iturrarán Viveros, 2001, Scattering and diffraction of SH waves by a finite crack: An analytical solution: Geophysical Journal International, **145**, 749–758, doi: 10.1046/j.1365-246x.2001.01426.x.
Sato, H., M. C. Fehler, and T. Maeda, 2012, Seismic wave propagation and scattering in the heterogeneous earth, 2nd ed.: Springer.
Simmons, G., and W. F. Brace, 1965, Comparison of static and dynamic measurements of compressibility of rocks: Journal of Geophysical Research, **70**, 5649–5656, doi: 10.1029/JZ070i022p05649.
Sinha, B. K., and T. J. Plona, 2001, Wave propagation in rocks with elastic-plastic deformations: Geophysics, **66**, 772–785, doi: 10.1190/1.1444967.
Song, Y., H. Hu, and J. W. Rudnicki, 2017, Normal compression wave scattering by a permeable crack in a fluid-saturated poroelastic solid: Acta Mechanica Sinica, **33**, 356–367, doi: 10.1007/s10409-016-0633-8.
Wang, Z. W., L. Y. Fu, J. Wei, W. Hou, J. Ba, and J. M. Carcione, 2019, On the Green function of the Lord-Shulman thermoelasticity equations: Geophysical Journal International, **220**, 393–403, doi: 10.1093/gji/ggz453.
Wei, J., L. Y. Fu, J. M. Carcione, and T. Han, 2022, Wave-induced thermal flux and scattering of P-waves in a medium with aligned circular cracks: Geophysics, **87**, no. 5, MR209–MR218, doi: 10.1190/geo2021-0616.1.
Wei, J., L. Y. Fu, T. Han, and J. M. Carcione, 2020b, Thermoelastic dispersion and attenuation of P and SV wave scattering by aligned fluid-saturated cracks of finite thickness in an isothermal elastic medium: Journal of Geophysical Research: Solid Earth, **125**, e2020JB019942, doi: 10.1029/2020JB019942.
Wei, J., L. Y. Fu, Z. W. Wang, J. Ba, and J. M. Carcione, 2020a, Green function of the Lord-Shulman thermo-poroelasticity theory: Geophysical Journal International, **221**, 1765–1776, doi: 10.1093/gji/ggaa100.
Winkler, K. W., and X. Liu, 1996, Measurements of third-order elastic constants in rocks: The Journal of the Acoustical Society of America, **100**, 1392–1398, doi: 10.1121/1.415986.
Winkler, K. W., and L. McGowan, 2004, Nonlinear acoustoelastic constants of dry and saturated rocks: Journal of Geophysical Research: Solid Earth, **109**, B10204, doi: 10.1029/2004JB003262.
Yamashita, T., 1990, Attenuation and dispersion of SH waves due to scattering by randomly distributed cracks: Pure and Applied Geophysics, **132**, 545–568, doi: 10.1007/BF00876929.
Zhu, A., and D. A. Wiens, 1991, Thermoelastic stress in oceanic lithosphere due to hotspot reheating: Journal of Geophysical Research: Solid Earth, **96**, 18323–18334, doi: 10.1029/91JB01907.
Zimmerman, R. W., W. H. Somerton, and M. S. King, 1986, Compressibility of porous rocks: Journal of Geophysical Research: Solid Earth, **91**, 12765–12777, doi: 10.1029/JB091iB12p12765.

Biographies and photographs of the authors are not available.

Queries

1. The running head title is too long for the space allotted. Please provide a shorter title (40 characters or less) for the running head.

2. Please check if the given authors' affiliations are set correctly.

3. Please check the sentence, "Therefore, it is important …" for clarity.

4. We have changed the citation of Simmons et al. (1965) to Simmons and Brace (1965) to match the reference list. Is this correct?

5. Please check that the change made to the sentence," The attenuation decreases with…" retains the intended meaning.

6. Please check that the changes made to the sentence "Figures 6, 7, 8, and 9 display the same quantities …" retain the intended meaning.

7. Please check that the changes made to the sentence "Figures 10 and 11 show the same quantities …" retain the intended meaning.

8. Please check that the changes made to the sentence, "Unlike the case of normal incidence …" retains the intended meaning.

9. We have changed the citation of Patterson et al. (2021) to Patterson and Driesner (2021) to match the reference list. Is this correct?

10. Unnumbered equations are not allowed by SEG style, so we have renumbered the equation as well as text citation. Please check the renumbering and the text mentions of the equations.

Funding Information

The following agencies have been identified as providing funding for your article. Please review the information carefully. If any changes are required, please submit those along with your other corrections to this article.

- National Natural Science Foundation of China (FundRef Registry ID: http://dx.doi.org/10.13039/501100001809)